

Learning to predict 3D rotational dynamics from images of a rigid body with unknown mass distribution

Justice J. Mason^{1,2*}
Princeton, NJ 08901

Christine Allen-Blanchette^{1*}
Princeton, NJ, 08901

Nicholas Zolman²
El Segundo, CA, 90245

Elizabeth Davison²
El Segundo, CA, 90245

Naomi Ehrlich Leonard¹
Princeton, NJ, 08901

¹Princeton University ²The Aerospace Corporation
{jjmason, cal5, naomi}@princeton.edu
{justice.j.mason, nicholas.f.zolman, elizabeth.davison}@aero.org

Abstract

In many real-world settings, image observations of freely rotating 3D rigid bodies, may be available when low-dimensional measurements are not. However, the high-dimensionality of image data precludes the use of classical estimation techniques to learn the dynamics. The usefulness of standard deep learning methods is also limited because an image of a rigid body reveals nothing about the distribution of mass inside the body, which, together with initial angular velocity, is what determines how the body will rotate. We present a physics-informed neural network model to estimate and predict 3D rotational dynamics from image sequences. We achieve this using a multi-stage prediction pipeline that maps individual images to a latent representation homeomorphic to $SO(3)$, computes angular velocities from latent pairs, and predicts future latent states using the Hamiltonian equations of motion. We demonstrate the efficacy of our approach on new rotating rigid-body datasets of sequences of synthetic images of rotating objects, including cubes, prisms and satellites, with unknown uniform and non-uniform mass distributions.

1 Introduction

Whether a freely rotating 3D rigid body tumbles unstably or spins stably depends on the distribution of mass inside the body and the body’s initial angular velocity (compare Figure 1(a) and (b)). This means that to predict the body’s rotational dynamics, it is not enough to know the external geometry of the body. That would be insufficient, for instance, to predict the different behavior of two bodies with the same external geometry and different internal mass distribution. Even if the bodies start at the same initial angular velocity, one body could tumble or wobble while the other spins stably; compare Figure 1(b) and (d).

Predicting 3D rigid body rotational dynamics is possible if the body’s mass distribution can be learned from observations of the body in motion. This is easier if the observations consist of low-dimensional data, e.g., measurements of the body’s angular velocity and the rotation matrix that defines the body’s orientation. It is much more challenging, however, if the only available measurements consist of images of the body in motion, as in the case of remote observations of a satellite.

In this paper, we address the challenge of learning and predicting 3D rotational dynamics from image sequences of a rigid body with unknown mass distribution and unknown initial angular velocity. To do so we design a neural network model that leverages Hamiltonian structure associated with 3D

rigid body dynamics. We show how our approach outperforms applicable methods from the existing literature.

Deep learning has proven to be an effective tool to learn dynamics from images. Previous work [54, 47, 4] has made significant progress in using physics-based priors to learn dynamics from images of 2D rigid bodies, such as a pendulum. Learning dynamics of 3D rigid-body motion has also been explored with various types of input data [11, 44, 18]. We believe our method is the first to use the Hamiltonian formalism to learn 3D rigid-body rotational dynamics from images.

To clarify the learning and prediction challenge addressed by our model, we review the equations from physics that describe the rotational dynamics of a 3D rigid body [22]. Let $\mathbf{J} \in \mathbb{R}^{3 \times 3}$ denote the *moment-of-inertia matrix* for a 3D rigid body. The matrix \mathbf{J} depends on how mass is distributed inside the body and can be understood to play a role in rotational dynamics that is analogous to, but more complicated than, the role played in translational dynamics of the scalar total body mass m . Define an orthonormal reference frame $\mathcal{B} = \{\mathbf{i}, \mathbf{j}, \mathbf{k}\}$ fixed to the body with origin at the body's center of mass. Let $\mathbf{r} = (x, y, z)$ be a point on the body expressed with respect to \mathcal{B} . The distribution of mass inside the rigid body is encoded by density $\rho(\mathbf{r})$, i.e., mass per unit volume of the body at the point \mathbf{r} . Let V be the total volume of the body and denote by \otimes the outer product. \mathbf{J} is computed [22] with respect to body frame \mathcal{B} as

$$\mathbf{J} = \iiint_V \rho(\mathbf{r})(\|\mathbf{r}\|^2 \mathbf{I}_3 - \mathbf{r} \otimes \mathbf{r}) dxdydz. \quad (1)$$

To get some intuition on the moment of inertia tensor, note that \mathbf{J} is a symmetric positive definite matrix, which means that it can always be diagonalized. If the frame \mathcal{B} is chosen so that \mathbf{J} is diagonal, the axes of \mathcal{B} are called the *principal axes* and the three diagonal elements of \mathbf{J} are called the *principal moments of inertia*.

Consider, for example, the rectangular prism of Figure 1(a) and (b) which has uniformly distributed mass, i.e., $\rho(\mathbf{r}) = \rho_0$ for every point \mathbf{r} in the body. Let \mathcal{B} be chosen with its first, second, and third axes aligned with the long, intermediate, and short axes of the prism, respectively. Then the axes of \mathcal{B} are the principle axes, $\mathbf{J} = \mathbf{J}_1$ is diagonal, and the first, second, and third principle moments of inertia (the diagonal elements of \mathbf{J}_1) are ordered from smallest to largest. For the very same rectangular prism but with the nonuniform distribution of mass used in Figure 1(d), the moment-of-inertia matrix \mathbf{J}_3 , with respect to the same frame \mathcal{B} , is no longer diagonal and its principle moments of inertia are different from those in the uniform case. \mathbf{J}_1 and \mathbf{J}_3 as well other moment-of-inertia matrices used for experiments in this work are given in Appendix A.1.

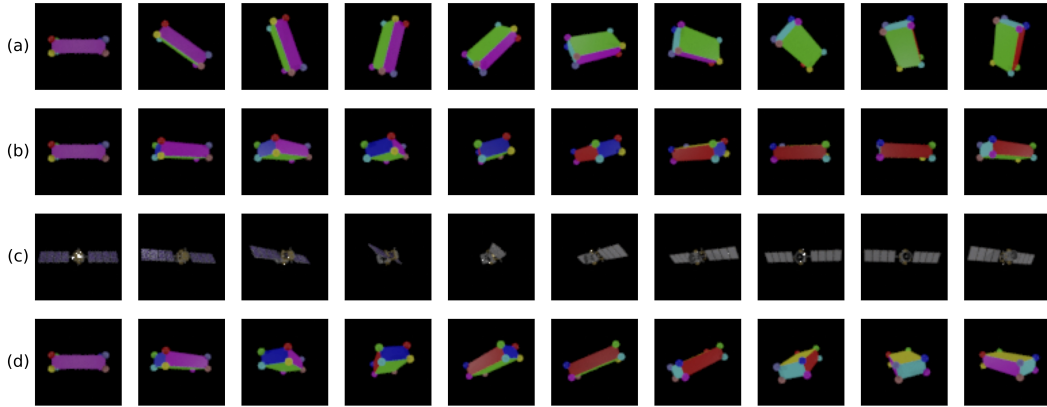


Figure 1: Simulations illustrating how mass distribution and initial angular velocity determine behavior. (a) Tumbling prism: uniform mass distribution ($\mathbf{J} = \mathbf{J}_1$) and initial angular velocity near an unstable solution. (b) Spinning prism: same uniform mass distribution ($\mathbf{J} = \mathbf{J}_1$) as (a) but with initial angular velocity near stable solution yields very different behavior from (a). (c) Spinning CALIPSO satellite: same mass distribution ($\mathbf{J} = \mathbf{J}_1$) and same initial angular velocity as (b) yields same behavior as (b) despite different exterior. (d) Wobbling prism: same initial velocity as (b) but different (nonuniform) mass distribution ($\mathbf{J} = \mathbf{J}_3$) yields different behavior from (b).

Let $\boldsymbol{\Omega}(t) \in \mathbb{R}^3$ denote the *body angular velocity*, i.e., the angular velocity of the body expressed with respect to \mathcal{B} , at time $t \geq 0$. Similarly, let $\boldsymbol{\Pi}(t) \in \mathbb{R}^3$ denote the *body angular momentum* at time $t \geq 0$, where $\boldsymbol{\Pi}(t) = \mathbf{J}\boldsymbol{\Omega}(t)$. Let $\boldsymbol{\Omega}_0 = \boldsymbol{\Omega}(0)$ be the initial body angular velocity.

Euler’s equations [22] describe the rotational dynamics of the body, i.e., the evolution over time t of $\boldsymbol{\Pi}$ given \mathbf{J} and $\boldsymbol{\Omega}_0$:

$$\frac{d\boldsymbol{\Pi}(t)}{dt} = \boldsymbol{\Pi}(t) \times \mathbf{J}^{-1}\boldsymbol{\Pi}(t), \quad \boldsymbol{\Pi}(0) = \mathbf{J}\boldsymbol{\Omega}_0, \quad (2)$$

where \times is the vector cross product. The corresponding evolution of body angular velocity over time is $\boldsymbol{\Omega}(t) = \mathbf{J}^{-1}\boldsymbol{\Pi}(t)$, where $\boldsymbol{\Pi}(t)$ is the solution of (2).

The orientation of the rigid body at time t is described by the rotation matrix $\mathbf{R}(t) \in \mathbf{SO}(3)$ that maps points on the body from body frame coordinates to inertial frame coordinates. $\mathbf{SO}(3) = \{\mathbf{R} \in \mathbb{R}^{3 \times 3} \mid \mathbf{R}^T \mathbf{R} = \mathbf{I}_3, \det(\mathbf{R}) = +1\}$ is the space of all 3D rotations. Given $\boldsymbol{\Omega}(t)$, $t \geq 0$, the evolution of orientation over time is computed from the rigid body kinematics equations:

$$\frac{d\mathbf{R}(t)}{dt} = \mathbf{R}(t) \boldsymbol{\Omega}_\times(t), \quad (3)$$

where $\boldsymbol{\Omega}_\times$ is the 3×3 skew-symmetric matrix defined by $(\boldsymbol{\Omega}_\times)\mathbf{y} = \boldsymbol{\Omega} \times \mathbf{y}$ for $\mathbf{y} \in \mathbb{R}^3$.

For the rotational dynamics (2), there are three equilibrium solutions, i.e., where $d\boldsymbol{\Pi}(t)/dt = 0$, corresponding to steady spin about the short principal axis, intermediate principal axis, and long principal axis, respectively. Steady spin about the short axis and long axis is stable, which means that an initial angular velocity near either of these solutions yields a spinning behavior, independent of exterior geometry, see Figure 1(b) and (c). Steady spin about the intermediate axis is unstable, which means that an initial angular velocity near this solution yields a tumbling behavior, see Figure 1(a).

Figure 1(a) and (b) show that for the same prism with the same (uniform) mass distribution and thus the same moment-of-inertia matrix \mathbf{J}_1 , different values of initial body angular velocity result in very different behavior: an unstable tumble in 1(a) and a stable spin in 1(b). Figure 1(b) and (d) show that for the same prism with the same initial angular velocity, different mass distributions yield different behaviors, a steady spin in (b) when $\mathbf{J} = \mathbf{J}_1$ and a wobble in (d) when $\mathbf{J} = \mathbf{J}_3$. Figure 1(b) and (c) show that the rotational dynamics of a rigid body with the same moment-of-inertia matrix \mathbf{J}_1 and same initial body angular velocity yield the same behavior, despite different exterior geometries, i.e., the prism in (b) and the CALIPSO [1] satellite in (d).

These cases illustrate that without a way of inferring the underlying mass distribution and estimating initial conditions, there is no way to predict the dynamics from images.

In this paper we introduce a model, with architecture depicted in Figure 2, that (1) learns 3D rigid-body rotational dynamics from images, (2) predicts future image sequences in time, and (3) generates a low-dimensional, interpretable representation of the latent state. Our model incorporates the Hamiltonian formulation of the dynamics as an inductive bias to facilitate learning the moment-of-inertia matrix, \mathbf{J} , and an auto-encoding map between images and $\mathbf{SO}(3)$. The efficacy of our approach is demonstrated through long-term image prediction on synthetic datasets. Due to scarcity of appropriate datasets, we have created publicly-available, synthetic datasets of rotating objects (e.g. cubes, prisms, and satellites) applicable for evaluation of our model as well as other tasks on 3D rigid-body rotation such as pose estimation.

2 Related work

A growing body of work incorporates Hamiltonian and Lagrangian formalisms to improve the accuracy and interpretability of learned representations in neural network based dynamical systems forecasting [23, 13, 16]. Greydanus et al. [23] predict symplectic gradients of a Hamiltonian system using a Hamiltonian parameterized by a neural network. They show that the Hamiltonian neural network predicts the evolution of conservative systems better than a baseline black-box model. Chen et al. [13] improve the long-term prediction performance of [23] by minimizing the MSE over predicted state trajectories rather than one-step symplectic gradients. Cranmer et al. [16] propose parameterization of the system Lagrangian by a neural network arguing that momentum coordinates may be difficult to compute in some settings. Each of the aforementioned learn from sequences of phase-space measurements, our model learns from images.

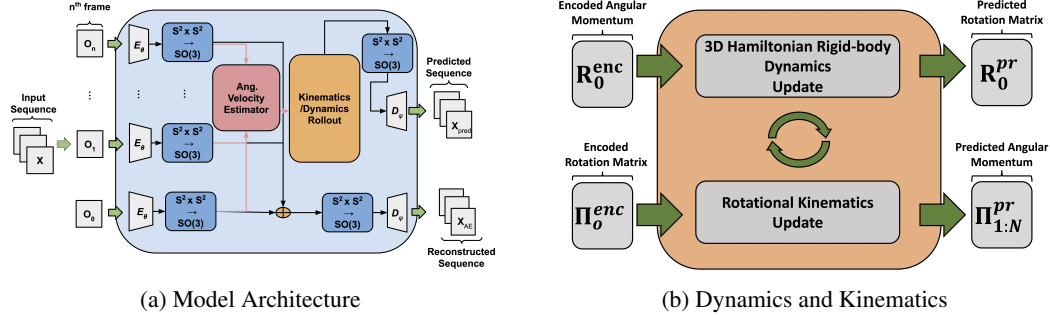


Figure 2: A schematic of the model architecture (left). The architecture combines an auto-encoding neural network with Hamiltonian dynamics for 3D rigid bodies (right). The encoder maps a sequence of images to a sequence of latent states in $\text{SO}(3)$. We estimate body angular velocities and momenta, then predict future orientation (\mathbf{R}) and momentum states ($\mathbf{\Pi}$) using the learned Hamiltonian. Each future latent state is decoded into an image using orientation states predicted by the learned dynamics.

The authors of [54, 4, 47] leverage Hamiltonian and Lagrangian neural networks to learn the dynamics of 2D rigid bodies (e.g., the planar pendulum) from image sequences. Zhong and Leonard [54] introduce a coordinate-aware VAE with a latent Lagrangian neural network (LNN) which learns the underlying dynamics and facilitates control. Allen-Blanchette et al. [4] use a latent LNN in an autoencoding neural network to learn dynamics without control or prior knowledge of the configuration-space structure. Toth et al. [47] use a latent Hamiltonian neural network in a VAE to learn dynamics without control, prior knowledge of the configuration-space structure or dimension. Similarly to Toth et al. [47], we use a latent Hamiltonian neural network to learn dynamics. Distinctly, however, we consider a 3D rigid body dynamics and incorporate prior knowledge of the configuration-space structure to ensure interpretability of the learned representations.

Others have considered the problem of learning 3D rigid-body dynamics [11, 44, 18]. Byravan and Fox [11] uses point-cloud data and action vectors (forces) as inputs to a black-box neural network to predict the resulting $\text{SE}(3)$ (rotation and translation) transformation matrix, which represents the motion of objects within the input scene. Peretroukhin et al. [44] create a novel symmetric matrix representation of $\text{SO}(3)$ and incorporate it into a neural network to do orientation prediction on synthetic point-cloud data and images. Duong and Atanasov [18] use low-dimensional measurement data (i.e. the rotation matrix and angular momenta) to learn rigid body dynamics on $\text{SO}(3)$ and $\text{SE}(3)$ for control.

The combination of deep learning with physics-based priors allows models to learn dynamics from high-dimensional data such as images [54, 47, 4]. However, as far as we know, our method is the first to use the Hamiltonian formalism to learn 3D rigid-body rotational dynamics from images.

3 Background

3.1 The $\mathcal{S}^2 \times \mathcal{S}^2$ parameterization of 3D rotation group $\text{SO}(3)$

The $\mathcal{S}^2 \times \mathcal{S}^2$ parameterization of the 3D rotation group $\text{SO}(3)$ is a surjective and differentiable mapping with a continuous right inverse [19]. Define the n -sphere: $\mathcal{S}^n = \{\mathbf{v} \in \mathbb{R}^{(n+1)} \mid v_1^2 + v_2^2 + \dots + v_{n+1}^2 = 1\}$. The $\mathcal{S}^2 \times \mathcal{S}^2$ parameterization of $\text{SO}(3)$ is given by $(u, v) \mapsto (w_1, w_2, w_3)$ with $w_1 = u$, $w_2 = v - v\langle u, v \rangle$, $w_3 = w_1 \times w_2$, where w_i are renormalized to have unit norm.

Intuitively, this mapping constructs an orthonormal frame from the unit vectors u and v by Gram-Schmidt orthogonalization. The right inverse of the parameterization is given by $(w_1, w_2, w_3) \mapsto (w_1, w_2)$. Other parameterizations of $\text{SO}(3)$ such as the exponential map ($\mathfrak{so}(3) \mapsto \text{SO}(3)$) and the quaternion map ($\mathcal{S}^3 \mapsto \text{SO}(3)$) do not have continuous inverses and therefore are more difficult to use in deep manifold regression [19, 34, 9].

3.2 3D rotating rigid-body kinematics

The orientation of a rotating 3D rigid body $\mathbf{R}(t) \in \mathbf{SO}(3)$ changing over time t can be computed from angular velocity $\boldsymbol{\Omega}(t)$ using the kinematic equations given by the time-rate-of-change of $\mathbf{R}(t)$ shown in equation (3). For computational purposes, 3D rigid-body rotational kinematics are commonly expressed in terms of the quaternion representation $\mathbf{q}(t) \in \mathcal{S}^3$ of the rigid-body orientation $\mathbf{R}(t)$. The kinematics (3) written in terms of quaternions [5] are

$$\frac{d\mathbf{q}(t)}{dt} = \mathbf{Q}(\boldsymbol{\Omega}(t))\mathbf{q}(t), \quad \mathbf{Q}(\boldsymbol{\Omega}) = \begin{pmatrix} -\boldsymbol{\Omega}_{\times} & \boldsymbol{\Omega} \\ -\boldsymbol{\Omega}^T & 0 \end{pmatrix}. \quad (4)$$

3.3 3D rigid-body dynamics in Hamiltonian form

The canonical Hamiltonian formulation derives the equations of motion for a mechanical system using only the symplectic form and a Hamiltonian function, which maps the state of the system to its total (kinetic plus potential) energy [22]. This formulation has been used by several authors to learn unknown dynamics: the Hamiltonian structure (canonical symplectic form) is used as a physics prior and the unknown dynamics are uncovered by learning the Hamiltonian [23, 56, 47]. Consider a system with configuration space \mathbb{R}^n and a choice of n generalized coordinates that represent configuration. Let $\mathbf{z}(t) \in \mathbb{R}^{2n}$ represent the vector of n generalized coordinates and their n conjugate momenta at time t . Define the Hamiltonian function $\mathcal{H} : \mathbb{R}^{2n} \mapsto \mathbb{R}$ such that $\mathcal{H}(\mathbf{z})$ is the sum of the kinetic plus potential energy. Then the equations of motion [22] derive as

$$\frac{d\mathbf{z}}{dt} = \Lambda_{\text{can}} \nabla_{\mathbf{z}} \mathcal{H}(\mathbf{z}), \quad \Lambda_{\text{can}} = \begin{pmatrix} \mathbf{0}_n & \mathbf{I}_n \\ -\mathbf{I}_n & \mathbf{0}_n \end{pmatrix} \quad (5)$$

where $\mathbf{0}_n \in \mathbb{R}^{n \times n}$ is the matrix of all zeros and Λ_{can} is the matrix representation of the *canonical symplectic form*.

The Hamiltonian equations of motion for a freely rotating 3D rigid body evolve on the 6-dimensional space $T^*\mathbf{SO}(3)$, the co-tangent bundle of $\mathbf{SO}(3)$. However, because of rotational symmetry in the dynamics, i.e., the invariance of the dynamics of a freely rotating rigid body to the choice of inertial frame, the Hamiltonian formulation of the dynamics can be reduced using the Lie-Poisson Reduction Theorem [39] to the space $\mathbb{R}^3 \sim \mathfrak{so}^*(3)$, the Lie co-algebra of $\mathbf{SO}(3)$. These reduced Hamiltonian dynamics are equivalent to (2), where body angular momentum is $\boldsymbol{\Pi}(t) \in \mathfrak{so}^*(3)$, for $t \geq 0$. The invariance can be seen by observing that the rotation matrix $\mathbf{R}(t)$, which describes the orientation of the body at time t , does not appear in (2). $\mathbf{R}(t)$ is calculated from the solution of (2) using (3).

The reduced Hamiltonian $h : \mathfrak{so}^*(3) \mapsto \mathbb{R}$ for the freely rotating 3D rigid body (just kinetic energy):

$$h(\boldsymbol{\Pi}) = \frac{1}{2} \boldsymbol{\Pi} \cdot \mathbf{J}^{-1} \boldsymbol{\Pi}. \quad (6)$$

The reduced Hamiltonian formulation [39] is

$$\frac{d\boldsymbol{\Pi}}{dt} = \Lambda_{\mathfrak{so}^*(3)}(\boldsymbol{\Pi}) \nabla_{\boldsymbol{\Pi}} h(\boldsymbol{\Pi}), \quad \Lambda_{\mathfrak{so}^*(3)}(\boldsymbol{\Pi}) = \boldsymbol{\Pi}_{\times}, \quad (7)$$

which can be seen to be equivalent to (2). The equations (7), called *Lie-Poisson equations*, generalize the canonical Hamiltonian formulation. The generalization allows for different symplectic forms, i.e., $\Lambda_{\mathfrak{so}^*(3)}$ instead of Λ_{can} in this case, each of which is only related to the latent space and symmetry. Our physics prior is the generalized symplectic form and learning the unknown dynamics means learning the reduced Hamiltonian. This is a generalization of the existing literature where dynamics of canonical Hamiltonian systems are learned with the canonical symplectic form as the physics prior [23, 16, 13, 47]. Using the generalized Hamiltonian formulation allows extension of the approach to a much larger class of systems than those described by Hamilton’s canonical equations, including rotating and translating 3D rigid bodies, rigid bodies in a gravitational field, multi-body systems, and more.

4 Learning Hamiltonian dynamics on $T^*\mathbf{SO}(3)$

In this section we outline our approach for learning and predicting rigid-body dynamics from image sequences. The multi-stage prediction pipeline maps individual images to an $\mathbf{SO}(3)$ latent space

where angular velocities are computed from latent pairs. Future latent states are computed using the generalized Hamiltonian equations of motion and a learned representation of the reduced Hamiltonian. Finally, the predicted latent representations are mapped to images giving a predicted image sequence.

4.1 Notation

N denotes the number of image sequences in the dataset, and $T + 1$ is the length of each image sequence. Image sequences are written $\mathbf{I}_k = \{I_0^k, \dots, I_T^k\}$, embedded sequences are written $Z_k = \{z_0^k, \dots, z_T^k\}$, $\mathbf{SO}(3)$ latent sequences of rotation matrices are written $\mathbf{R}_k = \{R_0^k, \dots, R_T^k\}$ with $R_t^k \in \mathbf{SO}(3)$, and quaternion latent sequences are written $\mathbf{q}_k = \{q_0^k, \dots, q_T^k\}$ with $q_t^k \in \mathcal{S}(3)$. Each element \mathbf{x}_t^k represents the quantity \mathbf{x} at time step t for sequence k from the dataset, where $k \in \{1, \dots, N\}$. Quantities generated with the learned dynamics are denoted with a hat (e.g., \hat{q}).

4.2 Embedding to an $\mathbf{SO}(3)$ latent space

We embed image observations of a rotating rigid body to an $\mathbf{SO}(3)$ latent space using the composition of functions $f \circ \pi \circ E_\theta : \mathcal{I} \mapsto \mathbf{SO}(3)$. The encoder network $E_\theta : \mathcal{I} \mapsto \mathbb{R}^6$ is learned during training, the projection $\pi : \mathbb{R}^6 \mapsto \mathcal{S}^2 \times \mathcal{S}^2$ is defined as $\pi(z) = (u/\|u\|, v/\|v\|)$, $u, v \in \mathbb{R}^3$ where $z = (u, v)$, and the function $f : \mathcal{S}^2 \times \mathcal{S}^2 \mapsto \mathbf{SO}(3)$ denotes the surjective and differentiable $\mathcal{S}^2 \times \mathcal{S}^2$ parameterization of $\mathbf{SO}(3)$ (see Section 3.1) which constrains embedded representations to the $\mathbf{SO}(3)$ manifold where we do reconstruction of the dynamics.

4.3 Hamiltonian dynamics on $T^*\mathbf{SO}(3)$

Following the reduction of $T^*\mathbf{SO}(3)$ described in Section 3.3, we predict future latent states on $\mathfrak{so}^*(3)$ and $\mathbf{SO}(3)$ using the reduced Hamiltonian dynamics (7) on $\mathfrak{so}^*(3) \sim \mathbb{R}^3$, the kinematic reconstruction (4) on \mathcal{S}^3 , and the learned moment-of-inertia matrix \mathbf{J}_ψ . We construct the initial condition $x_0^k = (q_0^k, \Pi_0^k) \in (\mathcal{S}^3, \mathbb{R}^3)$ using the pair of sequential $\mathbf{SO}(3)$ latent states (R_0^k, R_1^k) (see Section 4.2). The quaternion q_0^k is computed using the implementation of a modified Shepperd’s algorithm[38] and the angular momentum Π_0^k is computed as $\Pi_0^k = \mathbf{J}_\psi \Omega_0^k$ where the angular velocity Ω_0^k is approximated using the algorithm proposed in [27] (see Appendix A.6). The kinematic equations (4) are integrated forward using a Runge-Kutta fourth-order numerical solver (RK45) and a normalization step [5].

We decode an image sequence from the predicted quaternion sequence \mathbf{q}_k in three steps. We first transform each \hat{q}_t^k to $\hat{R}_t^k \in \mathbf{SO}(3)$, then apply the right inverse of the $\mathcal{S}^2 \times \mathcal{S}^2$ parameterization of $\mathbf{SO}(3)$, and finally, decode from $\mathcal{S}^2 \times \mathcal{S}^2$ with the decoding neural network D_ϕ .

4.4 Loss functions

In this section we describe each component of our loss function: the auto-encoder reconstruction loss \mathcal{L}_{ae} , prediction-base reconstruction loss $\mathcal{L}_{\text{pred}}$, and latent losses $\mathcal{L}_{\text{latent, R}}$ and $\mathcal{L}_{\text{latent, } \Pi}$. The function \mathcal{L}_{ae} ensures the embedding to $\mathbf{SO}(3)$ is sufficiently expressive to represent the entire image dataset, and $\mathcal{L}_{\text{pred}}$ ensures agreement between input image sequences and the predicted images sequences produced using the learned dynamics. Both $\mathcal{L}_{\text{latent, R}}$ and $\mathcal{L}_{\text{latent, } \Pi}$ ensure consistency between the encoded latent states given by the encoding pipeline and the predicted latent states given by the learned dynamics.

For notational convenience we denote the embedding pipeline $\mathcal{E} : \mathcal{I} \mapsto \mathcal{S}^3$ and the decoding pipeline $\mathcal{D} : \mathcal{S}^3 \mapsto \mathcal{I}$

Reconstruction losses The auto-encoding reconstruction loss is the mean square error (MSE) between the ground-truth image sequence and the reconstructed image sequence:

$$\mathcal{L}_{\text{ae}} = \frac{1}{NT} \sum_{k=1}^N \sum_{t=0}^{T-1} \|I_t^k - (\mathcal{D} \circ \mathcal{E})(I_t^k)\|_2^2.$$

The prediction-based reconstruction loss function is the MSE between the ground-truth image sequence and the predicted image sequence:

$$\mathcal{L}_{\text{pred}} = \frac{1}{NT} \sum_{k=1}^N \sum_{t=1}^T \|I_t^k - \mathcal{D}(\hat{q}_t^k)\|_2^2.$$

Latent losses One of the latent state losses is a distance metric on $\text{SO}(3)$ [27], defined as the MSE (using the Frobenius norm $\|\cdot\|_F$) between the 3×3 identity matrix and right-difference of the encoded latent states and the latent states predicted using the learned dynamics:

$$\mathcal{L}_{\text{latent, R}} = \frac{1}{NT} \sum_{k=1}^N \sum_{t=1}^T \|\mathbf{I}_3 - (R_{\text{enc}_t}^k)^T \hat{R}_t^k\|_F^2.$$

The other latent state loss is computed as the MSE of the angular momenta estimated using the encoded latent states (see Figure 2) and the predicted angular momenta:

$$\mathcal{L}_{\text{latent, } \Pi} = \frac{1}{NT} \sum_{k=1}^N \sum_{t=1}^T \|\Pi_{\text{enc}_t}^k - \hat{\Pi}_t^k\|_2^2.$$

5 3D rotating rigid-body datasets

To evaluate our model, we introduce six synthetic datasets of freely rotating objects. Previous efforts in learning dynamics from images [23, 47, 4, 54] consider only 2D planar systems (e.g., the simple pendulum, Acrobot, and cart-pole); and existing datasets of freely rotating rigid bodies in 3D such as SPEED [31, 46], SPEED+ [43], and URSO[45], contain random image-pose pairs rather than sequential pairs needed for video prediction and dynamics extraction. Our datasets showcase the rich dynamical behaviors of 3D rotational dynamics through images, capable of being used for 3D dynamics learning tasks. Furthermore, we acknowledge the need for applying our method to application-relevant images such as satellites. Accordingly, we have created the following new datasets on which we empirically test the performance of our model:

- **Uniform mass density cube:** Multi-colored cube of uniform mass density
- **Uniform mass density prism:** Multi-colored rectangular prism with uniform mass density
- **Non-uniform mass density cube:** Multi-colored cube with non-uniform mass density
- **Non-uniform mass density prism:** Multi-colored prism with non-uniform mass density
- **Uniform density synthetic-satellites:** Renderings of CALIPSO and CloudSat satellites with uniform mass density

The uniform mass density cube and prism datasets demonstrate baseline capabilities of our approach to do image prediction while the non-uniform density prism and uniform density satellite datasets are used to demonstrate capabilities of our model in scenarios of more complicated dynamics as explained in Section 1. For the uniform mass density cube dataset, inspired by Falorsi et al. [19], the angular momentum vector is constant for any initial condition. For every other dataset, including the uniform mass density prism, the full gamut of rigid rotational dynamics is possible, including stable spin as shown in Figure 1(b) and (c), wobble as shown in Figure 1(d) as well as unstable tumble as shown in Figure 1(a). The non-uniform mass density datasets validate the model’s capability to predict a change in mass distribution that may not be visible from the exterior, e.g., as part of failure diagnostics on a satellite where there may be broken or shifted internal components.

For each dataset, $N = 1000$ trajectories are created. Each trajectory consists of an initial condition $\mathbf{x}_0 = (\mathbf{R}_0, \Pi_0)$ that is integrated forward in time using a Python-based Runge-Kutta solver for $T = 100$ timesteps with spacing $\Delta t = 10^{-3}$. Initial conditions are chosen such that $(\mathbf{R}_0, \Pi_0) \sim \text{Uniform}(\text{SO}(3) \times S^2)$ with Π_0 scaled to have $\|\Pi_0\|_2 = 50$. The orientations $\hat{\mathbf{q}}$ from the integrated trajectories are passed to Blender [15] to render images of 28×28 pixels (as shown in Figure 1). At training time, each trajectory is snipped into sequences of length $\tau = 10$ using a sliding window, so that the model is trained on a batch of image sequences of length τ .

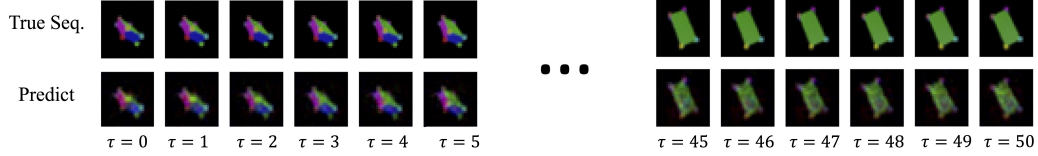


Figure 3: Predicted sequences for uniform mass density prism dataset given by our model. At prediction time, the model takes the first two images of a sequence, encodes them into the $\text{SO}(3)$ latent space and estimates the body angular momentum $\mathbf{A}.6$. The model predicts future latent states (using the estimated body angular momentum and first latent state as initial conditions), then the model decodes the predicted latent states into images. The prediction results show that the model is capable of predicting into the future at least five fold the time horizon used at training time.

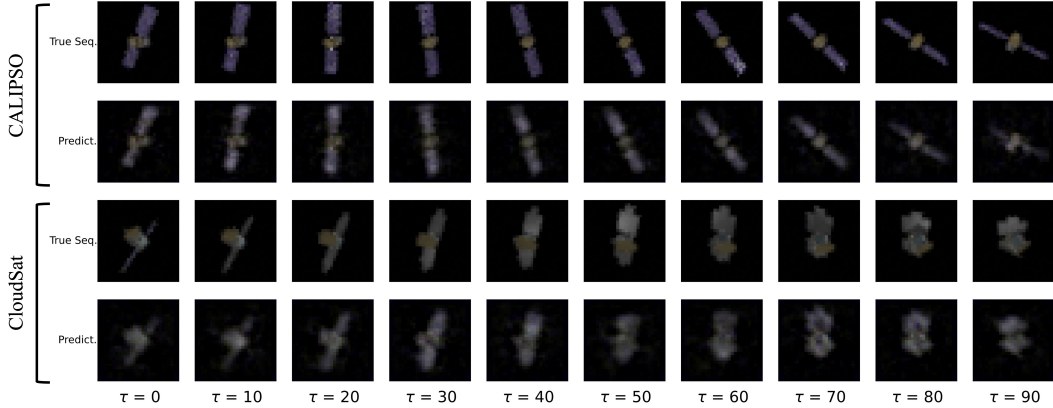


Figure 4: Predicted sequences for the CALIPSO satellite [1] (top) and CloudSat satellite [2] (bottom) with uniform mass densities given by our model. The prediction results show that the model is capable of predicting into the future with images of more complex geometries and surface properties at least ten fold the time horizon used at training time.

6 Results

6.1 Image prediction

A key contribution of this work is image prediction for freely rotating rigid bodies using the learned dynamics model. The model is capable of high-accuracy future prediction across six datasets. Figures 3 and 4 show the model’s performance on the datasets for both short and long-term predictions. The complete performance of our model on the cube and prism datasets is shown in Figure 5 in Appendix A.3. The model’s performance on the datasets is indicative of its capabilities to predict dynamics and map them to image space. Specifically, the model’s prediction performance on the non-uniform mass density datasets demonstrates its successful prediction when the mass distribution is visually ambiguous. This is particularly important because mass density (and thus rotational dynamics) is not something that can easily be inferred directly from images as we have discussed in Section 1. The model is compared to three baseline models: (1) an LSTM-baseline, (2) a Neural ODE [12]-baseline, and (3) the HGN [47] model. Recurrent neural networks like the LSTM-baseline provide a discrete dynamics model. Neural ODE can be combined with a multi-layer perceptron to model and predict continuous dynamics. HGN is a generative model with a Hamiltonian inductive bias. Architecture and training details for each baseline is given in Appendix A.4. The prediction performances of our model and the baselines are shown in Table 1. Our model outperforms the baseline models on the majority of the datasets with a more interpretable latent space, continuous dynamics, and fewer model parameters –motivating principles for this work.

Table 1: Average pixel mean square error over a 30-step prediction on the train and test data on six datasets. All values are multiplied by $1e+3$. We evaluate our model and compare to three baseline models: (1) recurrent model (LSTM [26]), (2) NeuralODE ([12]), (3) HGN ([47]). Our model outperforms all baseline models in the prediction task across the majority of the datasets. The number parameters for the dynamics models of each baselines are given in the last row of the table. Our model uses significantly fewer parameters to estimate the latent dynamics.

Dataset	Ours		LSTM - baseline		NeuralODE - baseline		HGN	
	TRAIN	TEST	TRAIN	TEST	TRAIN	TEST	TRAIN	TEST
Uniform Prism	2.66 \pm 0.10	2.71 \pm 0.08	3.46 \pm 0.59	3.47 \pm 0.61	3.96 \pm 0.68	4.00 \pm 0.68	4.18 \pm 0.0	7.80 \pm 0.30
Uniform Cube	3.54 \pm 0.17	3.97 \pm 0.16	21.55 \pm 1.98	21.64 \pm 2.12	9.48 \pm 1.19	9.43 \pm 1.20	17.43 \pm 0.00	18.69 \pm 0.12
Non-uniform Prism	4.27 \pm 0.18	6.61 \pm 0.88	4.50 \pm 1.31	4.52 \pm 1.34	4.67 \pm 0.58	4.75 \pm 0.59	6.16 \pm 0.08	8.33 \pm 0.26
Non-uniform Cube	6.24 \pm 0.29	4.85 \pm 0.35	7.47 \pm 0.51	7.51 \pm 0.50	7.89 \pm 1.50	7.94 \pm 1.59	14.11 \pm 0.13	18.14 \pm 0.36
Number of Parameters	6		52400		11400		-	

6.2 Latent space analysis and interpretability

Another contribution of this work is the interpretability of the latent space generated by our model from the image datasets. Black-box models with high-dimensional latent states make it very difficult to interpret and inspect the behavior of the latent space. Because our approach encodes all images into a latent space homeomorphic to $\text{SO}(3)$, we have convenient ways to interpret this low-dimensional space.

The form of our latent space provides us a way of inspecting the behavior of our model that previous works lack. In this sense, our approach provides a step towards producing new frameworks for interpreting deep learning models, analyzing failure modes, and using control for dynamic systems with significant structure from prior knowledge.

7 Conclusions

7.1 Summary

In this work, we have presented the first physics-informed deep learning framework for predicting image sequences of 3D rotating rigid-bodies by embedding the images as measurements in the configuration space $\text{SO}(3)$ and propagating the Hamiltonian dynamics forward in time. We have evaluated our approach on a new dataset of free-rotating 3D bodies with different inertial properties, and have demonstrated the ability to perform long-term image predictions.

By enforcing the representation of the latent space to be $\text{SO}(3)$, this work provides the advantage of interpretability over black-box physics-informed approaches. The extra interpretability of our approach is a step towards placing additional trust into sophisticated deep learning models. This work provides a natural path to investigating how to incorporate—and evaluate the effect of—classical model-based control directly to trajectories in the latent space. This interpretability is essential to deploying ML algorithms in safety-critical environments.

7.2 Limitations

While this approach has shown significant promise, it is important to highlight that this has only been tested in an idealized setting. Future work can examine the effect of dynamic scenes with variable backgrounds, lighting conditions, and multiple bodies. Perhaps more limiting, this approach currently relies on the ability to train the model for each system being examined; however future efforts can explore using transfer/few-shot learning between different 3D rigid-body systems.

7.3 Potential Negative Societal Impacts

While we do not believe this work directly facilitates injury to living beings, the inconsistency between the predicted latent representation and ground truth data may lead to unexpected results if deployed in real world environments.

7.4 Future work

Although our approach so far has been limited to embedding RGB-images of rotating rigid-bodies with configuration spaces in $\mathbf{SO}(3)$, it is important to note that there are natural extensions to a wider variety of problems. For instance, this framework can be extended to embed different high-dimensional sensor measurements—such as point clouds—by only modifying the feature extraction layers of the autoencoder. Likewise, depending on the rigid-body system, the latent space can be chosen to reflect the appropriate configuration space, such as generic rigid-bodies in $\mathbf{SE}(3)$ or systems in more complicated spaces, such as the n -jointed robotic arm on a restricted subspace of $\Pi_{i=1}^n(\mathbf{SO}(3))$.

References

- [1] Calipso: Cloud-aerosol lidar and infrared pathfinder satellite observations. URL https://www.nasa.gov/mission_pages/calipso/mission/index.html.
- [2] Cloudsat:. URL https://www.nasa.gov/mission_pages/calipso/mission/index.html.
- [3] Amir Ali Ahmadi and Bachir El Khadir. Learning dynamics systems with side information. In *Learning for Dynamics and Control*, June 2020.
- [4] Christine Allen-Blanchette, Sushant Veer, Anirudha Majumdar, and Naomi Ehrich Leonard. LagNetViP: A Lagrangian neural network for video prediction. *arXiv*, 2020.
- [5] Michael S. Andrieu and John L. Crassidis. Geometric integration of quaternions. *AIAA, Journal Guidance and Control*, 36(06):1762–1772, 2013. doi: <https://doi.org/10.2514/1.58558>.
- [6] Kendall A. Atkinson. *An introduction to numerical analysis*. John Wiley & Sons, 1989. ISBN 9780471500230.
- [7] Carles Balsells Rodas, Oleguer Canal Anton, and Federico Taschin. [re] hamiltonian generative networks. *ReScience C*, 7(2):#18, May 2021. doi: 10.5281/zenodo.4835278. URL <https://doi.org/10.5281/zenodo.4835278>.
- [8] Timothy Barfoot. *Robotic State Estimation*. Number 1107159393. Cambridge University Press, 1st edition, 2017.
- [9] Romain Brégier. Deep regression on manifolds: a 3d rotation case study. In *2021 International Conference on 3D Vision (3DV)*, pages 166–174. IEEE, 2021.
- [10] Steven L. Brunton, Joshua L. Proctor, and J. Nathan Kutz. Discovering governing equations from data by sparse identification of nonlinear dynamical systems. *Proceedings of the National Academy of Sciences*, 113(15):3932–3937, 2016. doi: 10.1073/pnas.1517384113. URL <https://www.pnas.org/doi/abs/10.1073/pnas.1517384113>.
- [11] Arunkumar Byravan and D. Fox. SE3-nets: Learning rigid body motion using deep neural networks. In *International Conference on Robotics and Automation*, 2017.
- [12] Ricky TQ Chen, Yulia Rubanova, Jesse Bettencourt, and David K Duvenaud. Neural ordinary differential equations. *Advances in neural information processing systems*, 31, 2018.
- [13] Zhengdao Chen, Jianyu Zhang, Martin Arjovsky, and Leon Bottou. Symplectic recurrent neural networks. In *International Conference on Learning Representations*, 2020.
- [14] Djork-Arné Clevert, Thomas Unterthiner, and Sepp Hochreiter. Fast and accurate deep network learning by exponential linear units (elus). *arXiv preprint arXiv:1511.07289*, 2015.
- [15] Blender Online Community. *Blender - a 3D modelling and rendering package*. Blender Foundation, Stichting Blender Foundation, Amsterdam, 2018. URL <http://www.blender.org>.
- [16] M. Cranmer, Sam Greydanus, Stephan Hoyer, Peter W. Battaglia, David N. Spergel, and Shirley Ho. Lagrangian neural networks. In *International Conference on Learning Representations*, 2020.
- [17] Miles Cranmer, Alvaro Sanchez-Gonzalez, Peter Battaglia, Rui Xu, Kyle Cranmer, David Spergel, and Shirley Ho. Discovering symbolic models from deep learning with inductive biases, 2020. URL <https://arxiv.org/abs/2006.11287>.
- [18] Thai Duong and Nikolay Atanasov. Hamiltonian-based neural ODE networks on the SE(3) manifold for dynamics learning and control. In *Proceedings of Robotics: Science and Systems*, July 2021.

- [19] Luca Falorsi, Pim de Haan, Tim R. Davidson, Nicola De Cao, Maurice Weiler, Patrick Forré, and Taco S. Cohen. Explorations in homeomorphic variational auto-encoding. *International Conference of Machine Learning Workshop on Theoretical Foundations and Application of Deep Generative Models*, 2018.
- [20] Marc Finzi, Ke Alexander Wang, and Andrew G Wilson. Simplifying Hamiltonian and Lagrangian neural networks via explicit constraints. *Conference on Neural Information Processing Systems*, 33(13880–13889):13, 2020.
- [21] Angel Flores-Abad, Ou Ma, Khanh Pham, and Steve Ulrich. A review of space robotics technologies for on-orbit servicing. *Progress in Aerospace Sciences*, 68:1–26, 2014. ISSN 0376-0421. doi: <https://doi.org/10.1016/j.paerosci.2014.03.002>. URL <https://www.sciencedirect.com/science/article/pii/S0376042114000347>.
- [22] Herbert Goldstein, Charles P. Poole, and John L. Safko. *Classical Mechanics*. Addison Wesley, 2002, 2002. ISBN 9780201657029.
- [23] Sam Greydanus, Misko Dzamba, and Jason Yosinski. Hamiltonian neural networks. *Conference on Neural Information Processing Systems*, abs/1906.01563, 2019.
- [24] Jayesh K. Gupta, Kunal Menda, Zhachary Manchester, and Mykel J. Kochenderfer. A general framework for structured learning of mechanical systems. *arXiv*, 2019.
- [25] Irina Higgins, David Amos, David Pfau, Sébastien Racanière, Loïc Matthey, Danilo Jimenez Rezende, and Alexander Lerchner. Towards a definition of disentangled representations. *ArXiv*, abs/1812.02230, 2018.
- [26] Sepp Hochreiter and Jürgen Schmidhuber. Long short-term memory. *Neural computation*, 9(8): 1735–1780, 1997.
- [27] Du Q. Huynh. Metrics for 3d rotations: Comparison and analysis. *Math Imaging Vis*, 35: 155–164, 2009. ISSN 0921-8890. doi: 10.1007/s10851-009-0161-2. URL <https://www.cs.cmu.edu/~cga/dynopt/readings/Rmetric.pdf>.
- [28] C. Kane, Jerrold E. Marsden, Michael Ortiz, and Matthew West. Variational integrators and the newmark algorithm for conservative and dissipative mechanical systems. *International Journal for Numerical Methods in Engineering*, 49:1295–1325, 2000.
- [29] Diederik P Kingma and Jimmy Ba. Adam: A method for stochastic optimization. *arXiv preprint arXiv: 1412.6980*, 2014.
- [30] Diederik P. Kingma and Max Welling. Auto-encoding variational Bayes. 2014.
- [31] Mate Kisantal, Sumant Sharma, Tae Ha Park, Dario Izzo, Marcus Martens, and Simone D’Amico. Satellite pose estimation challenge: Dataset, competition design, and results. *IEEE Transactions on Aerospace and Electronic Systems*, 56(5):4083–4098, oct 2020. doi: 10.1109/taes.2020.2989063. URL <https://doi.org/10.1109/taes.2020.2989063>.
- [32] Taeyoung Lee. *Computational geometric mechanics and control of rigid bodies*. PhD thesis, University of Michigan, 2008.
- [33] Taeyoung Lee, Melvin Leok, and N. Harris McClamroch. *Global Formulations of Lagrangian and Hamiltonian Dynamics on Manifolds*. 1860-6245. Springer, Cham, 2018.
- [34] Jake Levinson, Carlos Esteves, Kefan Chen, Noah Snively, Angjoo Kanazawa, Afshin Ros-tamizadeh, and Ameesh Makadia. An analysis of svd for deep rotation estimation. *Advances in Neural Information Processing Systems*, 33:22554–22565, 2020.
- [35] Yunzhu Li, Toru Lin, Kexin Yi, Daniel Bear, Daniel Yamins, Jiajun Wu, Joshua Tenenbaum, and Antonio Torralba. Visual grounding of learned physical models. In *International conference on machine learning*, pages 5927–5936. PMLR, 2020.
- [36] Michale Lutter, Christian Ritter, and Jan Petter. Deep Lagrangian networks: Using physics as model prior for deep learning. *International Conference of Learning Representations*, 2018.

- [37] C. Priyant Mark and Surekha Kamath. Review of active space debris removal methods. *Space Policy*, 47:194–206, 2019. ISSN 0265-9646. doi: <https://doi.org/10.1016/j.spacepol.2018.12.005>. URL <https://www.sciencedirect.com/science/article/pii/S0265964618300110>.
- [38] F. Landis Markley. Unit quaternion from rotation matrix. *AIAA, Journal Guidance and Control*, 31(02):440–442, 2008. doi: <https://doi.org/10.2514/1.31730>.
- [39] Jerrold E. Marsden and Tudor S. Ratiu. *Introduction to Mechanics and Symmetry*. Texts in Applied Mathematics. Springer New York, NY, 1999. ISBN 978-0-387-98643-2.
- [40] Jerrold E. Marsden and Matthew West. Discrete mechanics and variational integrators. *Acta Numerica*, 10:357 – 514, 2001.
- [41] Jürgen Moser and Alexander P. Veselov. Discrete versions of some classical integrable systems and factorization of matrix polynomials. *Communications in Mathematical Physics*, 139(2):217–243, 1991. doi: 10.1007/BF02352494. URL <https://doi.org/10.1007/BF02352494>.
- [42] Samuel E. Otto and Clarence W. Rowley. Linearly-recurrent autoencoder networks for learning dynamics. *ArXiv*, abs/1712.01378, 2019.
- [43] Tae Ha Park, Marcus Mörtens, Gurvan Lecuyer, Dario Izzo, and Simone D’Amico. Speed+: Next-generation dataset for spacecraft pose estimation across domain gap. In *2022 IEEE Aerospace Conference (AERO)*, pages 1–15, 2022. doi: 10.1109/AERO53065.2022.9843439.
- [44] Valentin Peretroukhin, Matthew Giamou, David M. Rosen, W. Nicholas Greene, Nicholas Roy, and Jonathan Kelly. A smooth representation of belief over $SO(3)$ for deep rotation learning with uncertainty. *CoRR*, abs/2006.01031, 2020. URL <https://arxiv.org/abs/2006.01031>.
- [45] Pedro F. Proença and Yang Gao. Deep learning for spacecraft pose estimation from photorealistic rendering. In *2020 IEEE International Conference on Robotics and Automation (ICRA)*, pages 6007–6013, 2020. doi: 10.1109/ICRA40945.2020.9197244.
- [46] Sumant Sharma, Connor Beierle, and Simone D’Amico. Pose estimation for non-cooperative spacecraft rendezvous using convolutional neural networks. In *2018 IEEE Aerospace Conference*, pages 1–12, 2018. doi: 10.1109/AERO.2018.8396425.
- [47] Peter Toth, Danilo J. Rezende, Andrew Jaegle, S ’ebastien Racanière, Aleksandar Botev, and Irina Higgins. Hamiltonian generative networks. In *International Conference on Learning Representations*, 2020.
- [48] Johan Verbeke and Ronald Cools. The newton-raphson method. *International Journal of Mathematical Education in Science and Technology*, 26:177–193, 1995.
- [49] Manuel Watter and Martin Riedmiller Jost Tobias Springenberg, Joschka Boedecker. Embed to control: A locally linear latent dynamics model for control from raw images. *Advances in neural information processing systems*, 27, 2015.
- [50] Jeffrey M. Wendlandt and Jerrold E. Marsden. Mechanical integrators derived from a discrete variational principle. *Physica D: Nonlinear Phenomena*, 106:223–246, 1997.
- [51] Jared Willard, Xiaowei Jia, Shaoming Xu, Michael S. Steinbach, and Vipin Kumar. Integrating scientific knowledge with machine learning for engineering and environmental systems. 2020.
- [52] B. Williams, P. Antreasian, E. Carranza, C. Jackman, J. Leonard, D. Nelson, B. Page, D. Stanbridge, D. Wibben, K. Williams, M. Moreau, K. Berry, K. Getzandanner, A. Liounis, A. Mashiku, D. Highsmith, B. Sutter, and D. S. Laurretta. OSIRIS-REx Flight Dynamics and Navigation Design. *Space Science Reviews*, 214(4):69, April 2018. ISSN 1572-9672. doi: 10.1007/s11214-018-0501-x. URL <https://doi.org/10.1007/s11214-018-0501-x>.

- [53] Linhui Xiao, Jinge Wang, Xiaosong Qiu, Zheng Rong, and Xudong Zou. Dynamic-slam: Semantic monocular visual localization and mapping based on deep learning in dynamic environment. *Robotics and Autonomous Systems*, 117:1–16, 2019. ISSN 0921-8890. doi: <https://doi.org/10.1016/j.robot.2019.03.012>. URL <https://www.sciencedirect.com/science/article/pii/S0921889018308029>.
- [54] Yaofend Desmond Zhong and Naomi Ehrich Leonard. Unsupervised learning of Lagrangian dynamics from images for prediction and control. In *Conference on Neural Information Processing Systems*, 2020.
- [55] Yaofend Desmond Zhong, Biswadip Dey, and Amit Chakraborty. Dissipative SymODEN: Encoding Hamiltonian dynamics with dissipation and control into deep learning. In *ICLR 2020 Workshop on Integration of Deep Neural Models and Differential Equations*, 2020.
- [56] Yaofend Desmond Zhong, Biswadip Dey, and Amit Chakraborty. Symplectic ODE-Net: Learning Hamiltonian dynamics with control. In *International Conference on Learning Representations*, 2020.
- [57] Yi Zhou, Connelly Barnes, Jingwan Lu, Jimei Yang, and Hao Li. On the continuity of rotation representations in neural networks. *2019 IEEE/CVF Conference on Computer Vision and Pattern Recognition (CVPR)*, pages 5738–5746, 2019.

A Supplementary materials

A.1 Dataset generation

Uniform mass density cube The moment-of-inertia tensor and its inverse for the uniform-mass-density cube are given by the matrices \mathbf{J}_0 and \mathbf{J}_0^{-1} in Table 2. The principle axes of rotation expressed in the body-fixed reference frame are also given in Table 2 showing the principle axes and body-fixed reference frame are aligned.

Uniform mass density prism The moment-of-inertia tensor and its inverse for the uniform-mass-density prism are given by the matrices \mathbf{J}_1 and \mathbf{J}_1^{-1} in Table 2. The principle axes of rotation expressed in the body-fixed reference frame are also given in Table 2 showing the principle axes and body-fixed reference frame are aligned.

Non-uniform mass density cube The moment-of-inertia tensor and its inverse for the non-uniform-mass-density cube are given by the matrices \mathbf{J}_2 and \mathbf{J}_2^{-1} in Table 2. The principle axes of rotation expressed in the body-fixed reference frame are also given in Table 2 and are not aligned with body-fixed reference frame.

Non-uniform density prism The moment-of-inertia tensor and its inverse for the non-uniform-mass-density prism are given by the matrices \mathbf{J}_3 and \mathbf{J}_3^{-1} in Table 2. The principle axes of rotation expressed in the body-fixed reference frame are also given in Table 2 and are not aligned with body-fixed reference frame.

CALIPSO [1] The moment-of-inertia tensor and its inverse for the CALIPSO satellite are given by the matrices \mathbf{J}_4 and \mathbf{J}_4^{-1} in Table 2. The principle axes of rotation expressed in the body-fixed reference frame are also given in Table 2, i.e., the principle axes and body-fixed reference frame are aligned.

CloudSat [2] The moment-of-inertia tensor and its inverse for the CloudSat satellite are given by the matrices \mathbf{J}_5 and \mathbf{J}_5^{-1} in Table 2. The principle axes of rotation expressed in the body-fixed reference frame are also given in Table 2, i.e., the principle axes and body-fixed reference frame are aligned.

Table 2: Table containing the moment-of-inertia tensors, inverse moment-of-inertia tensors, and principle axes used to generate training data for each object.

Object	Moment-of-Inertia Tensor	Inverse Moment-of-Inertia Tensor	Principle Axes
Uniform Cube	$\mathbf{J}_0 = \frac{1}{3} \begin{pmatrix} 1 & 0 & 0 \\ 0 & 1 & 0 \\ 0 & 0 & 1 \end{pmatrix}$	$\mathbf{J}_0^{-1} = \begin{pmatrix} 3 & 0 & 0 \\ 0 & 3 & 0 \\ 0 & 0 & 3 \end{pmatrix}$	$\left\{ \begin{pmatrix} 1 \\ 0 \\ 0 \end{pmatrix}, \begin{pmatrix} 0 \\ 1 \\ 0 \end{pmatrix}, \begin{pmatrix} 0 \\ 0 \\ 1 \end{pmatrix} \right\}$
Uniform Prism	$\mathbf{J}_1 = \begin{pmatrix} 0.42 & 0 & 0 \\ 0 & 1.41 & 0 \\ 0 & 0 & 1.67 \end{pmatrix}$	$\mathbf{J}_1^{-1} = \begin{pmatrix} 2.40 & 0 & 0 \\ 0 & 0.71 & 0 \\ 0 & 0 & 0.60 \end{pmatrix}$	$\left\{ \begin{pmatrix} 1 \\ 0 \\ 0 \end{pmatrix}, \begin{pmatrix} 0 \\ 1 \\ 0 \end{pmatrix}, \begin{pmatrix} 0 \\ 0 \\ 1 \end{pmatrix} \right\}$
Non-uniform Cube	$\mathbf{J}_2 = \begin{pmatrix} 0.17 & 0 & -0.56 \\ 0 & 0.17 & -0.99 \\ -0.56 & -0.99 & 0.17 \end{pmatrix}$	$\mathbf{J}_2^{-1} = \begin{pmatrix} 4.53 & -2.62 & -0.44 \\ -2.62 & 1.34 & -0.78 \\ -0.44 & -0.78 & -0.13 \end{pmatrix}$	$\left\{ \begin{pmatrix} -0.35 \\ -0.62 \\ -0.71 \end{pmatrix}, \begin{pmatrix} -0.87 \\ 0.49 \\ 0 \end{pmatrix}, \begin{pmatrix} -0.35 \\ -0.62 \\ 0.71 \end{pmatrix} \right\}$
Non-uniform Prism	$\mathbf{J}_3 = \begin{pmatrix} 0.47 & 0 & -0.28 \\ 0 & 1.61 & -0.49 \\ -0.28 & -0.49 & 1.83 \end{pmatrix}$	$\mathbf{J}_3^{-1} = \begin{pmatrix} 2.37 & 0.12 & 0.39 \\ 0.12 & 0.68 & 0.20 \\ 0.39 & 0.20 & 0.66 \end{pmatrix}$	$\left\{ \begin{pmatrix} -0.35 \\ -0.62 \\ -0.71 \end{pmatrix}, \begin{pmatrix} -0.87 \\ 0.49 \\ 0 \end{pmatrix}, \begin{pmatrix} -0.35 \\ -0.62 \\ 0.71 \end{pmatrix} \right\}$
CALIPSO	$\mathbf{J}_4 = \begin{pmatrix} 0.33 & 0 & 0 \\ 0 & 0.50 & 0 \\ 0 & 0 & 1.0 \end{pmatrix}$	$\mathbf{J}_4^{-1} = \begin{pmatrix} 3.0 & 0 & 0 \\ 0 & 2.0 & 0 \\ 0 & 0 & 1.0 \end{pmatrix}$	$\left\{ \begin{pmatrix} 1 \\ 0 \\ 0 \end{pmatrix}, \begin{pmatrix} 0 \\ 1 \\ 0 \end{pmatrix}, \begin{pmatrix} 0 \\ 0 \\ 1 \end{pmatrix} \right\}$
CloudSat	$\mathbf{J}_5 = \begin{pmatrix} 0.33 & 0 & 0 \\ 0 & 0.50 & 0 \\ 0 & 0 & 1.0 \end{pmatrix}$	$\mathbf{J}_5^{-1} = \begin{pmatrix} 3.0 & 0 & 0 \\ 0 & 2.0 & 0 \\ 0 & 0 & 1.0 \end{pmatrix}$	$\left\{ \begin{pmatrix} 1 \\ 0 \\ 0 \end{pmatrix}, \begin{pmatrix} 0 \\ 1 \\ 0 \end{pmatrix}, \begin{pmatrix} 0 \\ 0 \\ 1 \end{pmatrix} \right\}$

A.2 Training hyper-parameters

The training parameters used to run this experiment with the `train_dev.py` file is given in table 3.

Table 3: Hyper-parameters used to train model for the non-uniform mass density prism experiment. Only values differing from default values are given in table.

Experiment Training Parameters	
Parameter Name	Value
seed	0
gpu	'cuda:0'
test_split	0.2
val_split	0.1
n_epoch	1000
batch_size	256
learning_rate_ae	1E-3
learning_rate_dyn	1E-3
seq_len	10
time_step	1E-3
loss_gamma	1. 1. 1. 1.

A.3 Additional evaluation of model

The complete performance of the model on the uniform and non-uniform cube and prism datasets is given in Figure 5.

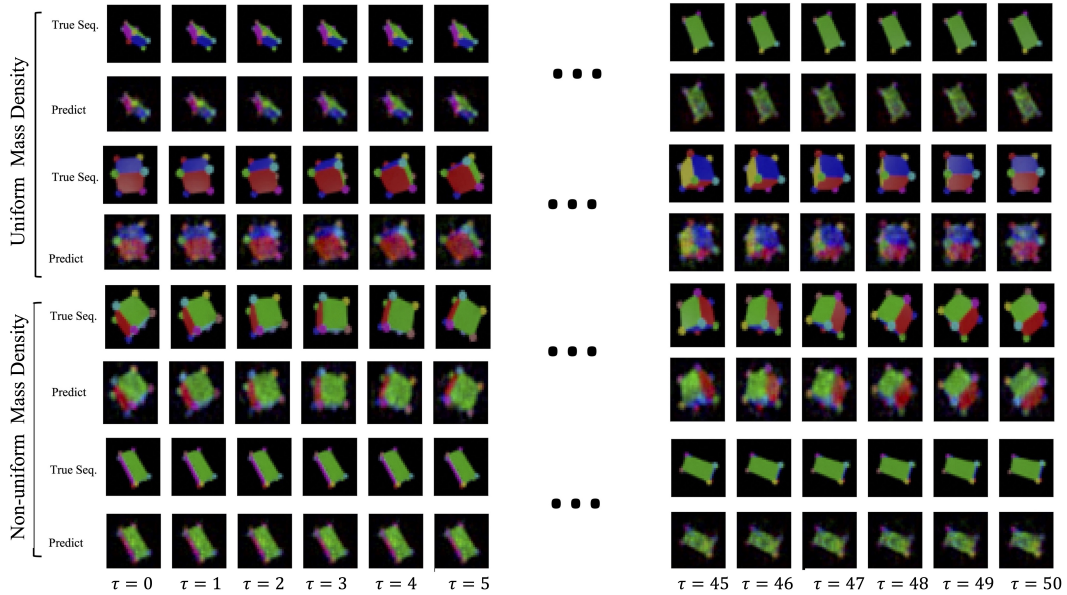


Figure 5: Predicted sequences for uniform and non-uniform mass density cube and prism datasets given by our model. At prediction time, the model takes the first two images of a sequence, encodes them into the $SO(3)$ latent space and estimates the body angular momentum A.6. The model predicts future latent states (using the estimated body angular momentum and first latent state as initial conditions), then the model decodes the predicted latent states into images. The prediction results show that the model is capable of predicting into the future at least five fold the time horizon used at training time.

A.4 Performance of baselines models

We compare the performance of our model against three baseline architectures: (1) an LSTM baseline, (2) a Neural ODE [12] baseline, and (3) Hamiltonian Generative Network (HGN) [47]. LSTM and NeuralODE baselines are trained using the same auto-encoder architecture as our model while HGN is trained with the auto-encoder architecture described in their work. The baselines differ from

our approach in how the dynamics are computed, emphasizing the beneficial role of Hamiltonian structure (LSTM- & NeuralODE-baseline) as well as our $\text{SO}(3)$ latent space (HGN).

LSTM - baseline The LSTM-baseline uses an LSTM network to predict the dynamics. The LSTM-baseline is a three-layer LSTM network with an input dimension of 6 and a hidden dimension of 50. The hidden state and cell state are randomly initialized and the output of the network is mapped to a 6-dimensional latent vector by a learned linear transformation. We train the LSTM-baseline to predict a single step from 9 sequential latent vectors by minimizing the sum of the autoencoder and dynamics losses, \mathcal{L}_{ae} and \mathcal{L}_{dyn} as defined in equations 4.4 and 4.4. At inference we use a recursive strategy to predict farther into the future by using each previous (predicted) state to predict the next. The qualitative performance for the LSTM-baseline is given in Figure 6, and the quantitative performance in terms of pixel mean-square error given in Table 1. The total number of parameters in the network is 52400.

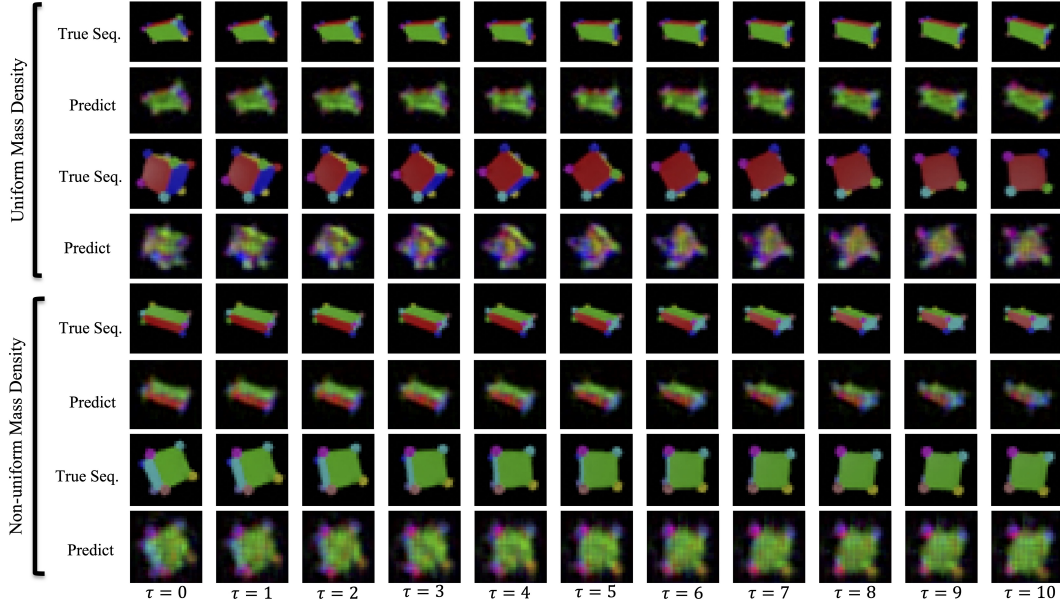


Figure 6: Predicted sequences for uniform/non-uniform prism and cube datasets given by the LSTM-baseline. At prediction time, the model takes the first 9 encoded latent states and predicts a sequence of 21 time steps recursively. The figure shows time steps 10-20, which are the first 11 predictions of the model. The LSTM-baseline has poorer performance than our proposed approach on all evaluated datasets.

Neural ODE [12] - baseline The Neural ODE-baseline uses the Neural ODE [12] framework to do prediction in the latent space. The Neural ODE-baseline is a three-layer MLP that uses the ELU [14] nonlinear activation function. The baseline has an input dimension of 6, a hidden dimension of 50, and an output dimension of 6. We train the Neural ODE-baseline to predict a sequence of latent states from a single latent state input by minimizing the sum of the auto-encoder and dynamics losses, \mathcal{L}_{ae} and $\mathcal{L}_{\text{pred}}$ as defined in Section 4.4. We use the RK4-integrator to integrate the learned dynamics. The qualitative performance for the NeuralODE-baseline is given in Figure 7, and the quantitative performance in terms of pixel mean-square error given in Table 1. The total number of parameters in the network is 11406.

Hamiltonian Generative Network (HGN) HGN [47] uses a combination of a variational auto-encoding (VAE) neural network, transformer, and Hamiltonian dynamics to do video prediction. When testing HGN as a baseline, we use the implementation provided by Balsells Rodas et al. [7]. During training, the same training hyperparameters are used as described in [47]. We train HGN on four of our datasets using their loss function (i.e. reconstruction and KL divergence). We use the Leap-frog integrator as this provided their model with its best performance on their datasets. The

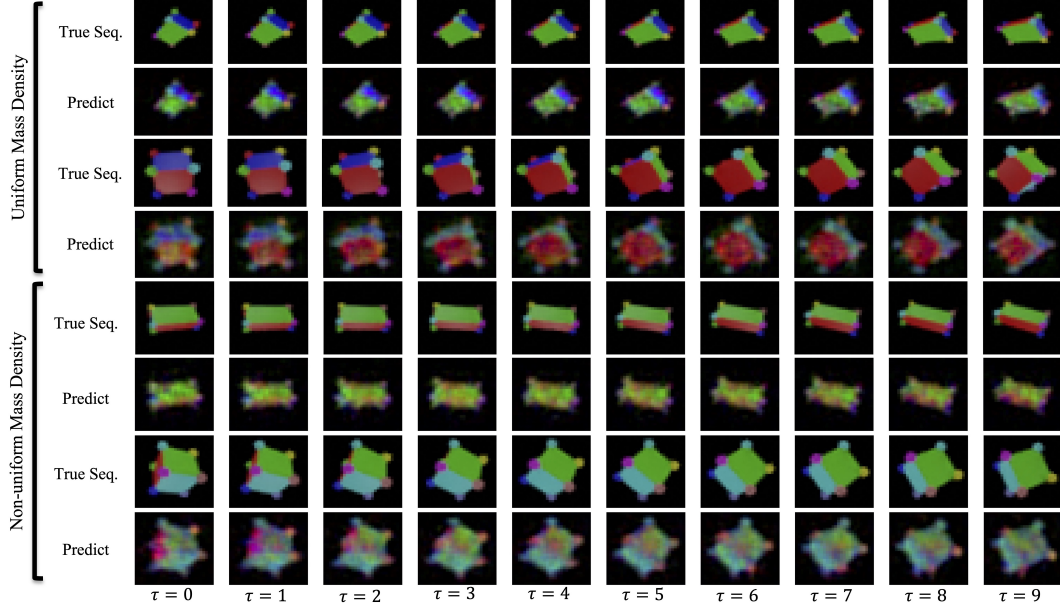


Figure 7: Predicted sequences for uniform/non-uniform prism and cube datasets given by the Neural ODE-baseline. At prediction time, the model takes the first encoded latent states and predicts a sequence of 10 steps recursively. The Neural ODE-baseline has poorer performance than the proposed approach on all datasets.

qualitative performance for HGN on our datasets is given in Appendix A.3, and the quantitative performance in terms of pixel mean-square error given in Table 1.

A.5 Ablation studies

In our ablation studies, we explore the impacts of the prediction loss 4.4 and latent losses on the image prediction performance of the proposed model. The ablated models are trained similarly to the proposed model, except for first ablation study only the prediction loss 4.4 is present in the total loss while for the second ablation study the latent losses 4.4 and 4.4 are removed. These ablation studies illuminate the influence of (1) the prediction loss 4.4 as well as (2) the latent losses 4.4 and 4.4 on our model’s prediction performance. From Table 4 and Figure 8, it is inferred that removing only

Table 4: Average pixel MSE over a 30 step unroll on the train and test data on four datasets for our ablative study. All values are multiplied by $1e+3$. We evaluate our proposed model and compare to a version of our model trained with only the prediction loss 4.4 and a version trained without the latent losses 4.4 and 4.4. Our full model outperforms or has comparable performance to the ablated models for the prediction task over all of our datasets.

Dataset	Ours		Ours - Prediction ONLY		Ours - Latent Ablation	
	TRAIN	TEST	TRAIN	TEST	TRAIN	TEST
Uniform Prism	3.03 ± 1.26	3.05 ± 1.21	3.99 ± 1.21	3.74 ± 0.93	3.99 ± 1.50	3.85 ± 1.45
Uniform Cube	4.13 ± 2.14	4.62 ± 2.02	5.73 ± 0.51	5.87 ± 0.56	7.11 ± 2.63	6.95 ± 2.41
Non-uniform Prism	4.98 ± 1.26	7.07 ± 1.88	4.27 ± 1.28	3.89 ± 1.10	3.86 ± 1.38	3.66 ± 1.27
Non-uniform Cube	7.27 ± 1.06	5.65 ± 1.50	6.23 ± 0.88	5.93 ± 0.85	-	-
CALIPSO	1.18 ± 0.43	1.19 ± 0.63	2.00 ± 0.78	1.85 ± 0.58	1.73 ± 0.73	1.62 ± 0.50
CloudSat	1.32 ± 0.74	1.56 ± 1.01	0.96 ± 0.17	1.39 ± 0.48	0.87 ± 0.29	1.40 ± 0.40

using the prediction loss slightly negatively affects the performance of our proposed model. While the prediction performance is slightly impacted, it is still strong (better than the baselines 1). This result also implies a slight positive impact from the auto-encoder and latent losses on the prediction performance. Furthermore, Table 4 and Figure 9 further corroborate the impact of the latent losses on prediction performance for our model. We see worsened average pixel MSE and future prediction. These results are further corroborated in the literature [4, 49].

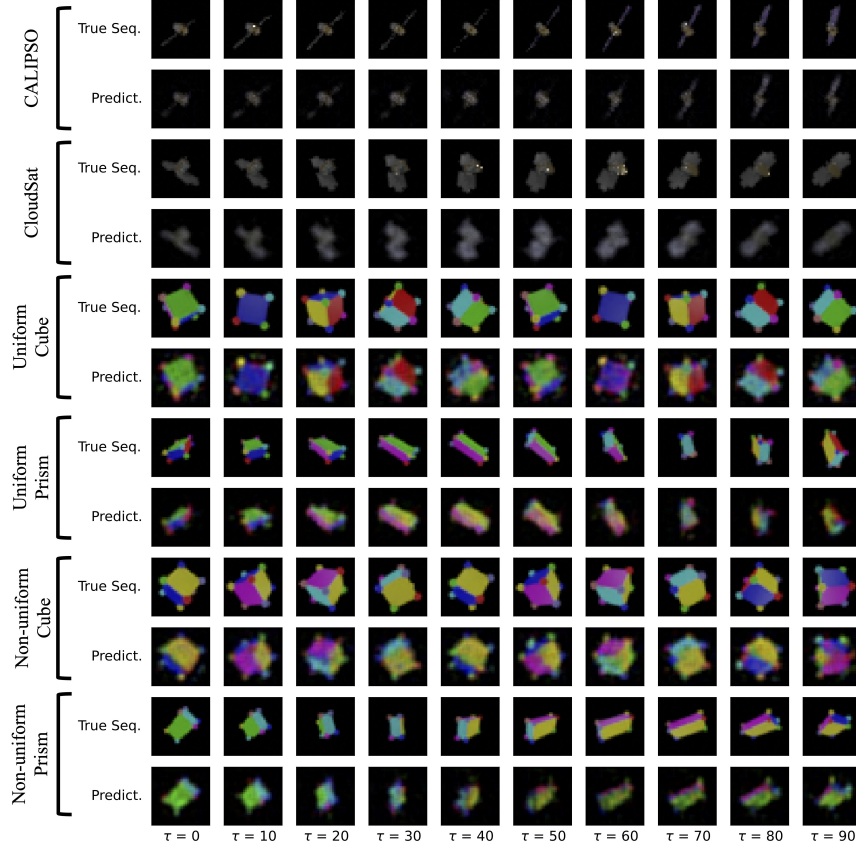


Figure 8: Evaluation of the image prediction performance of an ablated version of our model trained with the prediction loss 4.4 only. At prediction time, the model takes the first two encoded latent states and predicts a sequence of 100 steps recursively. The ablated model has poorer performance than the proposed approach over all datasets. The prediction performance worsens earlier than the proposed model’s performance as shown in Figures 3 and 5.

A.6 Body angular velocity estimator

The body angular velocity is the instantaneous rate of rotation of an object in its body-fixed reference frame. The body angular velocity is estimated using two sequential orientation matrices in the body-fixed frame, R_t and R_{t+1} . The first and second image frames of a given sequence are encoded into latent states, R_0 and R_1 , which are orientation matrices in the body-fixed frame. The angular velocity between frame 0 and frame 1 is calculated using Algorithm 1.

A.7 Compute resources & GPUs

The models are trained on a server with 8 NVIDIA A100 SXM4 GPUs. The processor is an AMD EPYC 7763, with 64 cores, 128 threads, 2.45 GHz base, 3.50 GHz boost, 256 MB cache, PCIe 4.0.

A.8 Code repository & dataset

The code repository and dataset used for this work will be released upon publication.

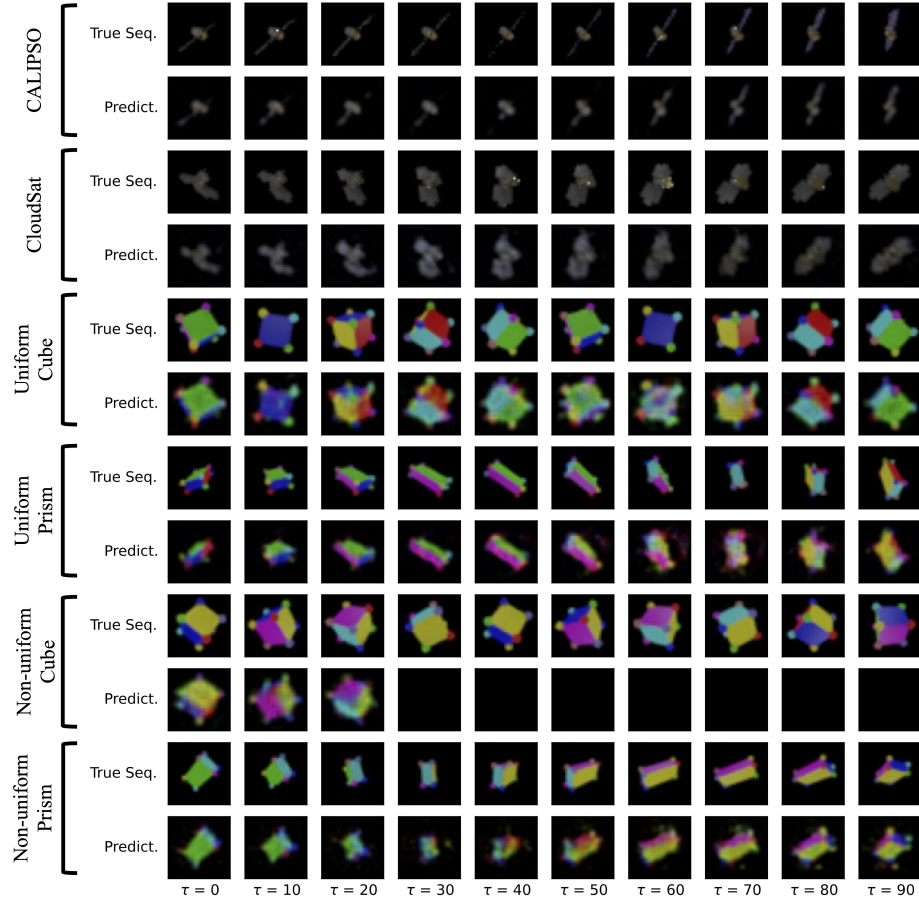


Figure 9: Evaluation of the image prediction performance of an ablated version of our model trained with the latent losses 4.4 and 4.4 removed. At prediction time, the model takes the first two encoded latent states and predicts a sequence of 100 steps recursively. The ablated model has poorer performance than the proposed approach over all datasets – even failing to predict after 30 timesteps for the non-uniform cube dataset. The prediction performance worsens earlier than the proposed model’s performance as shown in Figures 3 and 5.

Algorithm 1: An algorithm to calculate the body angular velocity given two sequential orientation matrices [27] and the time step in between them.

Data: $R_t, R_{t+1}, \Delta t$
Result: $\Omega_t = R_t \left(\frac{\theta}{\Delta t} \mathbf{u} \right)$
 $R_{\text{prod}} \leftarrow R_{t+1} (R_t^T);$
 $\mathbf{u}_\times \leftarrow R_{\text{prod}}^T - R_{\text{prod}};$
 $\theta \leftarrow \arccos \left(\frac{\text{Trace}(R_{\text{prod}}) - 1}{2} \right);$
if $\mathbf{u}_\times = \mathbf{0}$ **then**
 if $\theta = 0$ **then**
 $\mathbf{u} \leftarrow (1, 1, 1);$
 $\mathbf{u} \leftarrow \text{normalize}(\mathbf{u});$
 else
 if $\theta = \pi$ **then**
 $\mathbf{u} \leftarrow \text{column}(R_{\text{prod}} + \mathbb{I}_3);$
 $\mathbf{u} \leftarrow \text{normalize}(\mathbf{u});$
 end
 end
else
 if $\mathbf{u}_\times \neq \mathbf{0}$ **then**
 $\mathbf{u} \leftarrow \text{skew}^{-1}(\mathbf{u}_\times);$
 $\mathbf{u} \leftarrow \text{normalize}(\mathbf{u});$
 end
end
